*Article*

# A Methodology for Post-Necking Analysis in Isotropic Metals

**Martina Scapin** *[ID] **and Marta Beltramo** [ID]

Department of Mechanical and Aerospace Engineering, Politecnico di Torino, Corso Duca degli Abruzzi, 24, 10129 Turin, Italy; marta.beltramo@polito.it
* Correspondence: martina.scapin@polito.it

**Abstract:** Metallic materials are commonly characterized through tensile tests. For ductile metals, a consistent part of the test occurs after the necking onset. A first estimate of the post-necking behavior could be obtained by extrapolating the mathematical model that fits the pre-necking law. However, as well known, the accuracy of the predictions would not be guaranteed. Therefore, over the past decades many efforts have been devoted to dealing with the necking phenomenon. The most popular correction formula proposed by Bridgman is an analytical method based on the neck geometry. Despite being widely used, it may not be accurate at large strains due to the assumption of uniform distribution of the equivalent stress and equivalent strain in the specimen minimum cross-section. Starting from Bridgman's idea and in order to overcome its limitations, the present paper develops an efficient method to calibrate the hardening law of isotropic metallic materials at large strains. The proposed method requires to record the outer contour of the necking zone during the test and to build a dataset of necking deformed shapes. Experimental quasi-static tensile tests were analyzed with the proposed approach, which appears promising when critically compared with other methods.

**Keywords:** necking; strain-hardening; strength model identification; ductile metals; database; specimen deformed shape

## 1. Introduction

The tensile test is commonly used to characterize material strain hardening behavior. It owes its success to the ease of execution and to the fact that high deformation levels can be achieved before fracture. Thus, it offers a relatively easy way to investigate thermal effects, strain-rate sensitivity, ductile damage insurgence, etc.

During the first part of the test, thanks to the uniaxiality of the force and the specimen's smooth geometry, uniform deformation occurs within the gauge length. Therefore, the equivalent (Von Mises) stress $\sigma_{eq}$ and the axial stress $\sigma_a$ coincide. The same is valid for the strain, since elastic deformation can be reasonably neglected with respect to plastic deformation:

$$\sigma_{eq} = \sigma_a, \qquad \varepsilon_{eq} = \varepsilon_a. \tag{1}$$

Consider a cylindrical dog-bone specimen of initial gauge radius $r_0$ and initial gauge length $L_0$. Depending on the experimental setup and equipment, the axial stress and strain can be computed through the measured axial elongation $L$:

$$\sigma_a = \frac{F}{\pi r_0^2}\left(1 + \frac{\Delta L}{L_0}\right), \quad \varepsilon_a = \ln\left(1 + \frac{\Delta L}{L_0}\right), \tag{2}$$

or equivalently through the measured radial contraction (because of volume conservation in the plastic deformation of metals):

$$\sigma_a = \frac{F}{\pi r^2}, \quad \varepsilon_a = 2\ln\left(\frac{r_0}{r}\right). \tag{3}$$

However, the main issue regarding tensile tests on ductile metals is necking onset. This occurs soon after the maximum force, when the increase of stress cannot compensate for the reduction of the cross-section (this is known as the Considère condition [1]). During the post-necking phase, the specimen continues to deform while subjected to a decreasing load. Hence, necking may be seen as an unavoidable step towards fracture.

Nevertheless, the high deformations that the material exhibits during such phase are comparable to those that, in different loading conditions, could be reached in a stable way. Moreover, the post-necking phase constitutes the greater part of the test for ductile metals.

Therefore, over the past decades, many efforts have been devoted to dealing with the necking phenomenon. The aim was to exploit all the post-necking data of tensile tests to identify the material behavior at large strains. The difficulty is that as soon as necking initiates, the stress state becomes increasingly non-uniform and triaxial. Thus, the hypotheses at the basis of Equations (2) and (3) are not satisfied anymore. Moreover, an exact analytical solution for necking has not been found yet, so there are no exact equations that replace the previous ones to determine the post-necking $\sigma_{eq} - \varepsilon_{eq}$ curve. A first estimate of the post-necking behavior could be obtained by extrapolating the mathematical law that fits the pre-necking $\sigma_{eq} - \varepsilon_{eq}$ curve, but the accuracy of the predictions could not be guaranteed [2–4]. Moreover, this would not be possible for materials which reach the instability condition soon after yielding.

Therefore, many identification strategies have been proposed in the literature, as better detailed in Section Literature Review. One of the first correction formulae was proposed by Bridgman [5] and was based on the neck geometry (i.e., the curvature and the minimum radius). Many researchers found that Bridgman's theory, despite being widely used, may not be accurate at large strains [6,7] due to the assumption of uniform distribution of $\sigma_{eq}$ and $\varepsilon_{eq}$ in the specimen's minimum cross-section. Several analytical solutions have been developed to obtain better results. However, correction formulae are still based on a local evaluation of the specimen shape. Such measurements cannot be easily performed and there is no common agreement on how to do it.

The aim of this paper is to propose an efficient method that improves previous approaches in terms of accuracy and robustness. A certain number of post-necking deformed configurations were analyzed via a numerical database that established a relationship between the external profile and the hardening law. Since the database collected FE results, the accuracy with respect to Bridgman-like approaches would be improved. Moreover, considering a wider portion of the sample, and not just the necking center, can lead to a more robust and stable method. From the experimental point of view, the effort of the proposed method is limited, since it is enough to measure the force and record the specimen shape evolution. No speckle on the sample surface is required because just the external profile is needed. This can be determined as the boundary between the specimen and the background by digitally analyzing images.

In Section 2, the method proposed in this paper is presented. In Section 3, the experimental setup is described, focusing the attention on the imaging apparatus. In Section 4, the proposed method is applied to an experimental case study and compared with analytical methods. The experimental test considered was characterized by a necking onset that occurs soon after yielding: those are the situations in which post-necking identification strategies are of utmost importance. The aim is not to characterize a specific material, but to show how the proposed procedure works and what may be its potential in post-necking identification. Finally, in Section 5, a preliminary investigation for applying the proposed method to strain-rate sensitive materials is presented.

*Literature Review*

Several analytical identification strategies have been proposed in the past decades. Generally, they use Equation (3) at the minimum cross-section to estimate the average equivalent strain in that section. As observed in [2,8], Equation (2) fails to represent any local strain soon after the necking onset. Conversely, Equation (3) may still be representative

of a local strain as long as the strains distribution over the neck section does not undergo significant gradients.

For what $\sigma_{eq}$ is concerned with, different methods propose to determine an average value at the minimum cross-section by correcting the axial stress estimated at the minimum cross-section from Equation (3). From now on, the true stress and true strain, computed by applying Equation (3) at the minimum cross-section, will be indicated as $\sigma_t$ and $\varepsilon_t$.

The most common correction formula was proposed by Bridgman [5] and is reported hereinafter:

$$\sigma_{eq} = \frac{\sigma_t}{\left(1 + \frac{2R}{r}\right)\ln\left(1 + \frac{r}{2R}\right)},$$  (4)

where $R$ is the radius of curvature in a certain surrounding of the neck.

As already mentioned, Bridgman's correction is not very accurate at large strains [6,7]. The error is mainly introduced by the assumption of uniform $\sigma_{eq}$ and $\varepsilon_{eq}$ in the minimum cross-section. For improving the accuracy, similar analytical solutions have been proposed in the literature. A comprehensive review of these methods was provided by Gromada et al. [9]. According to the numerical analyses carried out by [9] on different hardening behaviors, other correction formulae give better results with respect to Bridgman. In particular, the one proposed by Gromada et al. [9] is the following:

$$\sigma_{eq} = \frac{\sigma_t}{\xi},$$

$$\text{being } \xi = 1 - \frac{5\Lambda}{7(1+5\Lambda)} - \frac{2(1-6\Lambda)}{7(1+5\Lambda)} + \frac{2}{7} + \frac{30\Lambda(8\Lambda-\delta-5\delta\Lambda)}{49\delta(1+5\Lambda)^2}$$
$$+ \frac{3(8\Lambda-\delta-5\delta\Lambda)}{7\delta(1+5\Lambda)}\left(\frac{2(1-6\Lambda)}{7(1+5\Lambda)} - \frac{2}{7}\right.$$
$$\left. - \frac{30\Lambda(8\Lambda-\delta-5\delta\Lambda)}{49\delta(1+5\Lambda)^2}\right)\ln\left|1 + \frac{7\delta(1+5\Lambda)}{3(8\Lambda-\delta-5\delta\Lambda)}\right|,$$
$$\Lambda = 1 - r_0/r,$$
$$\delta = r/R.$$  (5)

However, as stated by Tu et al. [2], the accuracy of the different correction formulae for a certain material is still not clear, so the choice of the formula is somewhat arbitrary.

From the experimental point of view, previous methods require measuring the minimum radius $r$ and the necking curvature radius $R$. The first can be measured through a linear variable displacement transducer [10] or by digitally analyzing images [11–13]. Conversely, it is very difficult to directly measure the instantaneous necking curvature since the neck position is random in a smooth specimen. Usually, necking profiles are obtained by digitally analyzing images, then they are fitted with functions, and finally the curvature is computed [7,12–14]. In some studies, 3D geometry information of the necking region has been used for estimating $r$ and $R$. For example, Siegmann et al. [14] used fringe projection together with Digital Image Correlation (DIC), whereas Chen and Pan [15] employed a mirror-assisted multi-view DIC technique. Versaillot et al. [16] combined stereo-DIC with Bridgman's theory. Overall, these strategies required a complex and advanced setup.

It can be concluded that all Bridgman-like approaches are affected by the experimental effort and uncertainty of measuring the radius of curvature $R$.

To overcome this issue, attempts have been conducted to establish a relation between $R$ and $r$ so that just the measurement of $r$ is required. This approach was suggested by Bridgman himself [5]. This was further developed by Le Roy et al. [17], who proposed a linear relationship between $r/R$ and $\varepsilon_t - \varepsilon_n$ (where $\varepsilon_n$ denotes the equivalent strain at the necking onset). Recently, Lu et al. [18] proposed a new two-parameter curve for the $r/R$ relationship. Mirone [19] conducted a numerical analysis, looking for a material-independent relationship that relates $\sigma_t$ to $\sigma_{eq}$ without the need to measure $R$. The result was the polynomial $\text{MLR}_\sigma$ which transforms $\sigma_t$ into the equivalent stress averaged on the neck cross-section for virtually all the materials satisfying the Von Mises plasticity. This polynomial is a function of $\varepsilon_t - \varepsilon_n$ because the necking governing variable is just the amount of plastic deformation after the necking onset.

As observed in [19], it is worth highlighting that when all the previous models are used to identify the plastic flow curve, they determine local variables, $\sigma_{eq}$ and $\varepsilon_{eq}$, by correcting global variables, $\sigma_t$ and $\varepsilon_t$. This association between global and local variables is implicitly based on the following hypothesis: the material point $r^*$ of the minimum cross-section which is characterized by $\sigma_{eq}(r^*) = \sigma_t$ is also characterized by having $\varepsilon_{eq}(r^*) = \varepsilon_t$. However, to the best of the authors' knowledge, this situation may not always be valid.

Thus, post-necking identification strategies that use FE simulations have been proposed to properly take into account triaxiality and non-uniformity. These approaches are known as FE-based inverse methods and consist of a recursive comparison between measured quantities and the corresponding predicted ones. Such quantities may be: the total axial force at given displacement increments beyond the maximum force [20–24], the specimen necking shape after the maximum force [25,26], and the shape along with the force time history [27,28]. Since an optimization is required, such approaches are more computationally expensive than analytical corrections. Conversely, the experimental effort is limited because the measurement of the curvature is not needed.

One may also cite FE-based inverse methods having as target the full-field strains of the necking region together with force time history [29–31] or strategies based on the principle of virtual work coupled with full-field measurements [32–34]. However, measuring full-field strains requires using DIC. This implies creating a speckle or deposited pattern on the specimen surface and recording it during the test, which could be difficult at very large strains, at high temperature, and/or at high strain-rate.

The previous literature review shows that many approaches take into account the time evolution of the necking geometry (in a smaller or wider specimen region). Conversely, in [26] the authors proposed a different approach to identify the plastic flow curve of isotropic metals in quasi-static tensile tests: instead of looking at the time evolution, they focused on a single time instant. The method exploits the fact that a single necking deformed shape intrinsically contains all the post-necking deformation history without looking explicitly at the time. A FE-based inverse method was employed. On one hand, such strategy took advantage of not having simplifying hypotheses on the stress and strain fields. On the other hand, it was characterized by a higher computational cost with respect to analytical methods.

Considering the amount of information that could be gained from a necking profile, the present paper developed Bridgman's idea further to improve it in terms of accuracy, gained knowledge and stability, as will be detailed later.

## 2. Proposed Method

In this work, an evolution of Bridgman's theory is proposed. It considers the whole shape at different time instants (instead of just the necking center) and each configuration is correlated to the material hardening behavior through the use of a database.

As proved in [26], a correlation exists between the necking deformed shape and the hardening law (for test conditions and/or materials in which temperature and strain-rate dependence can be considered negligible). Thus, from each necking configuration it is possible to estimate the hardening law in the corresponding range of the post-necking strains achieved. Hence, using a sequence of configurations leads to a series of hardening laws. Of course, the range of post-necking strains of a certain configuration is all contained in the range of post-necking strains of a subsequent configuration. This creates redundancy and improves the overall stability and robustness of the method.

### 2.1. Database Establishment

A database was employed to associate necking profiles with hardening laws. This was established through FE simulations of tensile tests to avoid introducing simplifying hypotheses on stress and strain states. Numerical tensile tests were characterized by different plastic flow curves (linear, power-law, and saturating). Then, post-necking hardening

laws and the corresponding results in terms of post-necking engineering curve and necking profiles were collected in a database.

Focusing on modeling details, a non-linear FE analysis must be performed since large strains were achieved, hence the general-purpose software Ansys LS-DYNA R14.0.0 was chosen. Exploiting the symmetries of the geometry and the material isotropy, a 2D axisymmetric model of a quarter of the sample was considered. Axisymmetric shell elements with one integration point were adopted. A symmetry constraint was applied at one end and a prescribed speed to the other end. In particular, since the explicit solver was used, it was checked that the prescribed motion did not introduce inertial effects. Furthermore, when simulating necking, techniques capable of limiting the element distortion were essential. Thus, a model with variable mesh was employed (analogous mesh have been commonly used since Tvergaard and Needleman [35]). A study on mesh size convergence was conducted to adequately chose the element size.

For what the material model is concerned with, different hardening curves were used. Other material properties, e.g., density, Young's modulus, and Poisson's ratio, have a negligible effect in quasi-static tests when large deformations are experienced. As will be clearer from Section 2.2, what matters is considering different shapes of the post-necking hardening law (regardless of the absolute stress values and the pre-necking behavior). Hence, in case of the power-law model, for example, changing the hardening exponent was enough to obtain all the possible shapes of the post-necking plastic flow curve.

*2.2. Procedure*

As anticipated, the identification strategy consisted of applying a certain procedure to different necking configurations. Such procedure is schematically depicted in Figure 1. Figure 1a,b graphically represent the procedure in the ideal case in which there exists a virtual material in the database (lighter curve) with the same post-necking behavior of the real one (darker line). Figure 1c summarizes the general procedure with a flowchart.

The algorithm firstly searches within the database for the numerical profile which is closer to the experimental one in terms of shape, regardless of the absolute size. This is shown in Figure 1a as "operation a1". There exists a numerical profile that, when equally scaled in both radial and axial coordinates, becomes overlapped with the experimental contour. Indeed, it is the relative shape that gives useful information on the post-necking hardening behavior. Conversely, the absolute size depends on the specimen size at the necking onset (i.e., on the initial size and necking onset). This consideration is based on the fact that the necking governing variable is $\varepsilon_{eq,pl} - \varepsilon_n$ and not $\varepsilon_{eq,pl}$.

Once the best shape in the database was chosen, the corresponding plastic flow curve was the one that, among all those considered, best represented the material plastic flow curve (just for the shape of the post-necking phase). This is highlighted in Figure 1b where "operation b2" horizontally translates the database to compensate for the different amount of uniform deformation (between the real material and that selected from the database). Of course, the experimental curve shown in Figure 1b would not be known in a real case, but it would be the result of the procedure.

Finally, since the shape does not give any information about the absolute stress level, the experimental force was compared with the force associated with the numerical shape. This allows to adequately scale stress values of the identified hardening law, as shown in Figure 1b, "operation b3".

Applying this procedure to a certain number of necking configurations leads to a series of laws, that could be properly averaged to identify a unique hardening law.
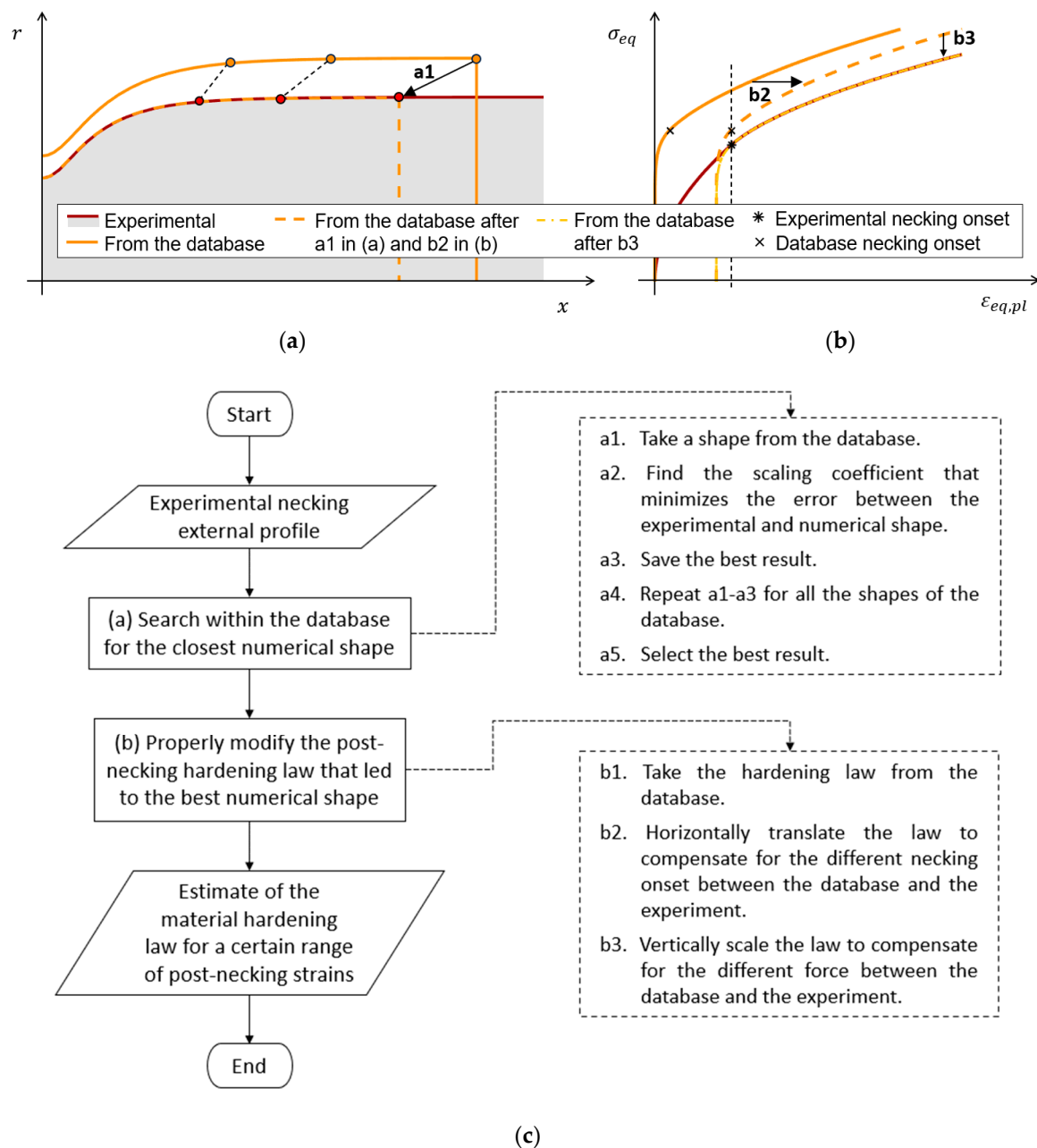
**Figure 1.** Schematic representation of the procedure. (**a**) compares the experimental and numerical shape before and after operation a1 (scaling of the numerical shape). (**b**) shows the operations to be performed on the database law to estimate the experimental one (horizontally translate and vertically scale). (**c**) is the flowchart representing the procedure to be applied to each necking configuration of interest.

## 3. Experimental Setup

Quasi-static tensile tests were conducted on a standard electromechanical testing machine, Zwick-Z100 (ZwickRoell GmbH & Co. KG, Ulm, Denmark), at a testing speed of 0.005 mm/s and at room temperature. Cylindrical dog-bone specimens were characterized by a 3 mm gauge diameter and a 5 mm gauge length (as those used in previous studies [36]). The load applied by the testing equipment was acquired and a high-resolution camera (ITA81-GM-20C by Opto Engineering, Mantova, Italy) was used to record the tests. Load data were gathered synchronously with image grabbing, because a time mismatch would lead to significant errors in the identification.

The measurement of the profile was essential in the proposed procedure. Hence, special care was taken in the imaging setup, not only for what the resolution was concerned with, but also for image distortion, and perspective errors. These latter factors are typical of common entocentric optics and may limit measurement accuracy and repeatability.

Such problems could be reduced by using telecentric lenses, as done by Zhang et al. [37]. These lenses, thanks to the path of rays within the optical system, allow the collecting of only ray cones whose principal ray is parallel to the opto-mechanical main axis. However, other accuracy issues may arise if the lens is only telecentric in object space: ray cones that enter parallelly can still reach the detector from different angles. To overcome this issue, bi-telecentric lenses could be used: being telecentric in both object and image space, principal rays are parallel when both entering and exiting the lens.

In addition, another limitation of common entocentric optics is the edge position uncertainty in backlighting. In such imaging setup, all rays collected by the lens are considered as coming from behind the object, so as part of the background. However, depending on the lighting source and on the object geometry, it could happen that some of these rays are actually rays reflected by the object surface. Thus, some portions of the object appear as part of the background, causing imprecise and unstable measurements. In contrast, telecentric lenses allow only reflected rays nearly parallel to the optical main axis to reach the detector. Hence, the risk of jeopardizing the measurement accuracy because of reflections from the object surface would be reduced. To further improve this aspect, telecentric lenses could be interfaced with a collimated illuminator. Only "expected" rays are collected by the lens and delivered onto the detector, thus significantly limiting border effects. This also ensures a high signal-to-noise ratio.

For all the above-mentioned reasons, the camera was mounted on the telecentric optical bench TCBENCH036 (by Opto Engineering, Mantova, Italy), which was equipped with a bi-telecentric lens coupled with a collimated illuminator. This allowed for the obtainment of high contrast images with the lowest possible geometrical distortion and perspective error. Such equipment requires an experimental setup where the workpiece is interposed between the camera and the illuminator, as shown in Figure 2. For what the focusing is concerned with, this must not be on the specimen front surface, but on its silhouette profile. This is an advantage of procedures based on the sample external contour.
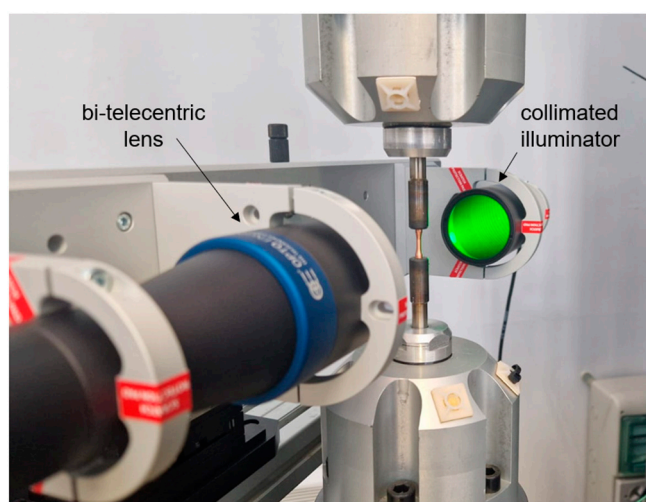


**Figure 2.** Experimental setup with the telecentric optical bench.

Recorded images were post-processed in the programming environment MATLAB R2023b to extract the specimen external contour. To this aim, several edge detection algorithms have been proposed in the previous research [11–13]. The present authors used the MATLAB function "imsegkmeans" to segment the interest area from the background. More specifically, this function implements an image segmentation technique based on

k-means clustering [38]. Finally, specimen edges were detected. In Figure 3, some frames of the acquired sequence are reported, showing the images' high quality and the profiles extracted.
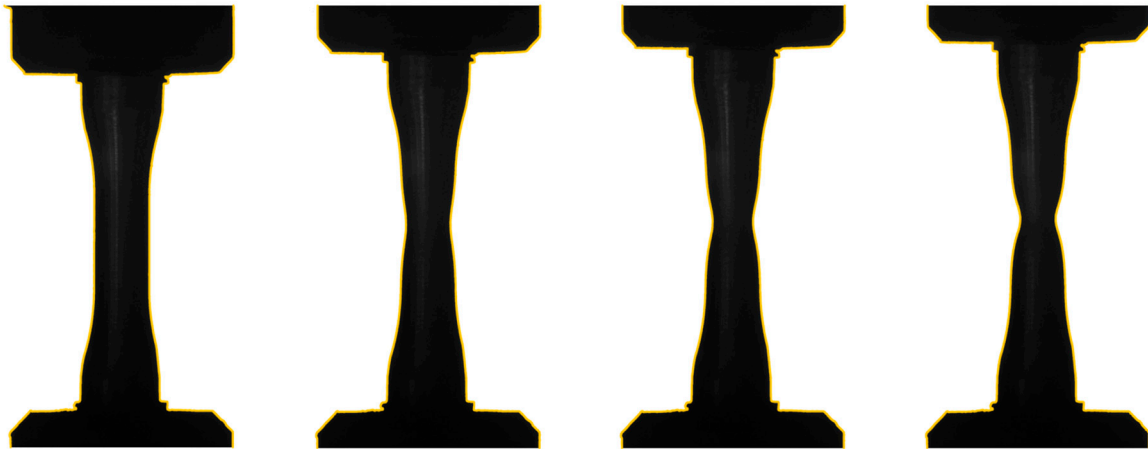


**Figure 3.** Sequence of images acquired by the camera mounted on the telecentric optical bench. The profile determined as external contour is highlighted.

## 4. Data Analysis for a Strain-Rate Insensitive Material

The experimental case that was analyzed was a quasi-static tensile test on pure copper. The reason is that it is a well-known and widely studied material [12,36,39] which exhibits low strain-rate sensitivity. Thus, as will be explained in Section 5, the material can be reasonably considered strain-rate insensitive within a test. Finally, being a pure metal, ductile damage is limited and the material experiences high strains before fracture.

In all the following paragraphs the authors did not consider the whole experimental test. The analysis was focused on the phase sufficiently far from a relevant reduction of the mechanical strength so that to limit the effect of void nucleation and coalescence [35].

The test was analyzed with Bridgman's theory to present the limitations caused by curvature measurements. Then, the proposed method was applied, and it was compared with Bridgman's and Gromada's prediction. For evaluating the accuracy of the different strategies, the hardening law that was taken as reference was firstly identified with a FE-based inverse method (as described in Section 4.1).

Since all these methods rely on material isotropy, this hypothesis needed to be verified. A top view of the fractured sample, as shown in Figure 4a, qualitatively suggests the isotropic behavior. To quantitatively check the isotropy, preliminary analyses were conducted: tensile tests were interrupted before fracture and CT scan analyses performed (see Figure 4b). The comparison of different projections of the CT scan indicated that the maximum deviation from the average profile was lower than 2.5%. Hence, the isotropy assumption is reasonable, and axisymmetric models can be used.
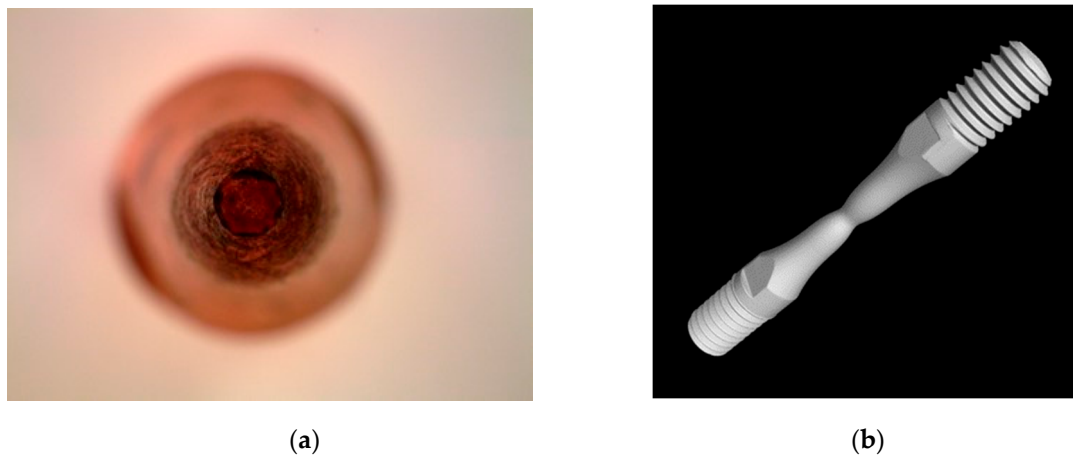
(**a**)



(**b**)

**Figure 4.** (**a**) Top view of the fractured copper specimen, acquired with an optical microscope. (**b**) 3D reconstruction of copper deformed specimen, made via a CT scan.

### 4.1. Reference Law

A FE-based inverse method, having the force at given increments of radial contraction as the target, was used to firstly identify the hardening law. Such approach required an optimization, which was implemented on the commercial program Ansys LS-OPT 7.0. A metamodel-based optimization was used and a sequential strategy with domain reduction was chosen. For what the model parametrization was concerned with, the hardening law was modeled as a piecewise linear function (*MAT_024 in Ansys LS-DYNA), whose slopes were the optimization variables.

For FE modeling, the same modeling choices described in Section 2.1 were adopted. The 2D axisymmetric model of a quarter of the specimen is shown in Figure 5. This picture aims to show the technique adopted for limiting element distortion. In the region where necking would develop, the mesh had smaller elements with an initial aspect-ratio such that, during necking development, a regular element shape was obtained.
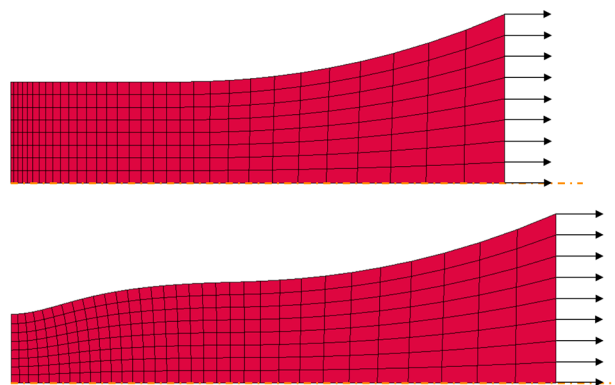


**Figure 5.** FE model of the specimen, showing the initial mesh and the necking deformed mesh.

The law identified via the FE-based inverse method will be used in Section 4.3 for evaluating analytical corrections and the proposed method. Such law can be considered as reference because, thanks to FE simulations, the specimen geometry, the strain field, and the stress field properly take into account non-uniformity and triaxiality. Moreover, the accuracy of the identified law is proved by the fact that this can adequately reproduce the experimental test, in terms of both the necking shape (as will be shown in Figures 6a and 7a) and the engineering curve (as will be shown in Figure 7b).

### 4.2. Bridgman's Correction

As mentioned in the introduction, several analytical approaches require the determination of the time evolution of the radius *r* of the minimum cross-section and the radius *R* of curvature in the necking center. However, measuring *R* is not straightforward and there is no common agreement on how to conduct it. Moreover, its estimation is mainly based on a local evaluation of the shape. The uncertainty in estimating *R* leads in turn to uncertainties in the identified law.

The analysis presented in this section investigates whether Bridgman's theory may predict different hardening laws, depending on the procedure used to estimate *R*. For each configuration under analysis, the average necking semi-profile was fitted with a polynomial function (as done in [7], for example). The curvature was approximated with the curvature of such function in the center of the necking. Then, the true curve was corrected according to Equation (4). The previous procedure was repeated by performing the fit on different specimen portions and adopting different orders for the polynomial. This investigated how much these choices affected Bridgman's prediction. The results are summarized in Figure 6.

Figure 6a shows, for a certain necking configuration, how the circle osculating the necking center changes when using polynomials of second, third, and fourth order. The different plots refer to different possible surroundings of the necking center to be considered for the fitting. The wider region (denoted as "Region 1") is defined as all the points that satisfy the condition $2\ln(r_0/r) > \varepsilon_n$.

Once the region of interest is chosen, an improvement of the prediction can be obtained by increasing the polynomial order. From Figure 6a, it can be seen that higher orders lead to an osculating circle that better approximates the profile. First of all, it is worth underlining that, when considering wider regions (as Region 1 and Region 2 of Figure 6a), the polynomial order must be able to catch at least the inflection points that may be present. The second order polynomial cannot have any inflection points; thus, it would not give acceptable results. Indeed, in Figure 6b, it is shown that the predicted law is affected by a considerable amount of error with respect to the reference one. Figure 6b also presents Bridgman's predictions in case of fitting Region 1 with third and fourth order polynomials. Both are able to catch inflection points but give two different results, highlighting that higher polynomial orders lead to hardening laws progressively closer to the reference one.

Simultaneously, once the order of the polynomial is fixed, the reduction of the fitting region improves the prediction of the osculating circle. However, if the region considered was too small, the polynomial would be badly conditioned and unstable results would be obtained (this mainly occurs with higher order polynomials). Nevertheless, it is difficult to know a priori the most adequate surrounding of the neck center. The consequent uncertainty can be seen in Figure 6c where the gray zone represents the variability of Bridgman's prediction when a third order polynomial was used for fitting different specimen portions. Such gray region did not consider unstable results, but one of them is shown for sake of completeness (dots of Figure 6c).

Overall, it can be concluded that Bridgman's correction gives good results at intermediate strains provided that an adequate fitting is performed. However, it was shown that even the best prediction of Bridgman's has a certain error at large strains, as already observed in [6,7]. The reason is that non-uniformity of $\sigma_{eq}$ and $\varepsilon_{eq}$ becomes relevant at large strains. This is an intrinsic error of Bridgman's theory that cannot be solved with a proper fitting of the profile. As stated in Section Literature Review, other analytical corrections are available in the literature for reducing this error, but the uncertainty of determining *R* remains. The issue is that it is difficult to know a priori which combination of polynomial order and analyzed portion will lead to better results.
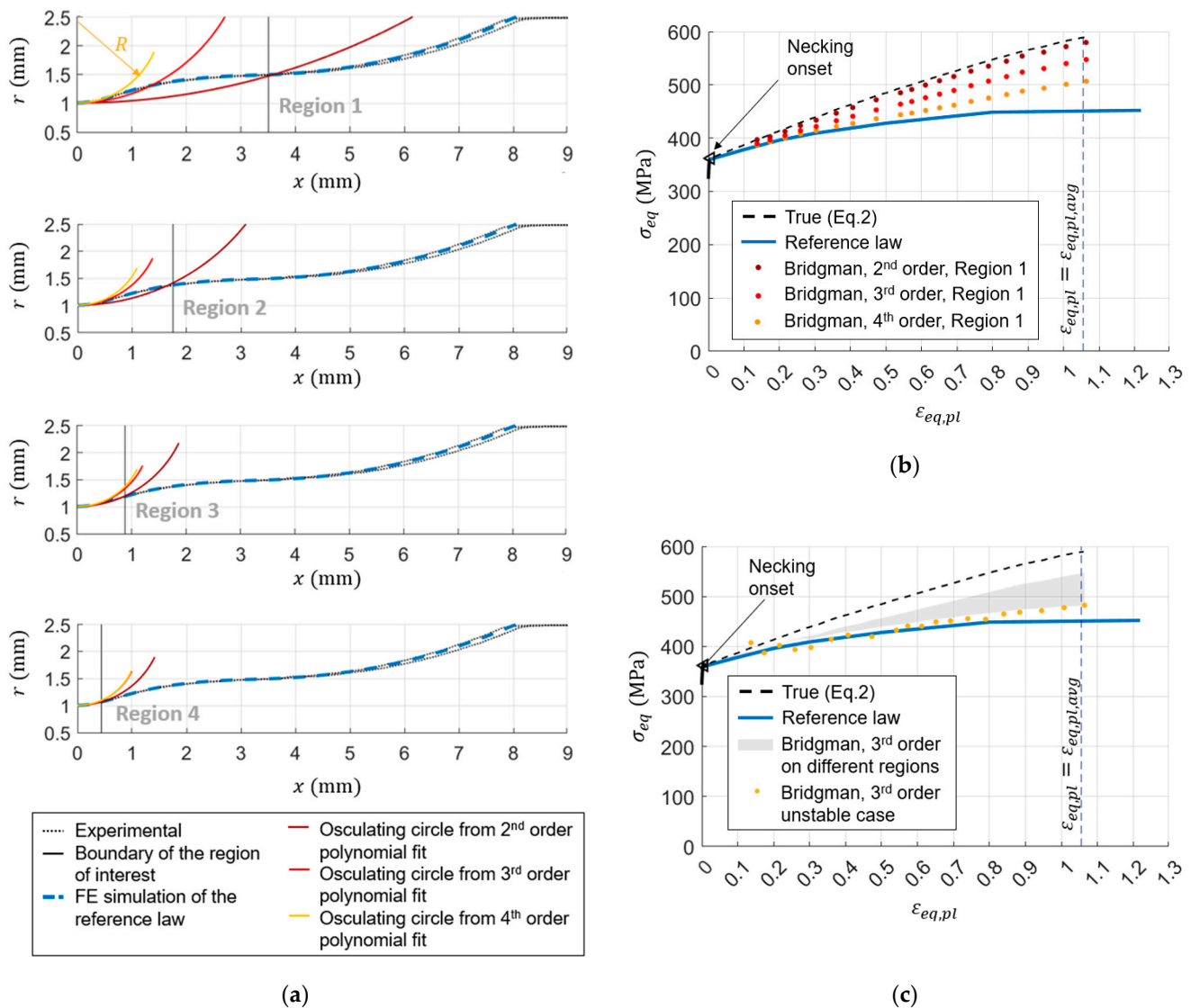
**Figure 6.** Analysis on Bridgman's correction. (**a**) Comparison between the experimental semi-profile, the one predicted by the reference law and the osculating circles obtained with different fitting choices; the four plots refer to the same configuration $\varepsilon_t = 0.8$ but differ for the region considered for fitting. (**b**) Comparison between the reference law and Bridgman's prediction when changing the polynomial order for fitting Region 1 of the specimen. (**c**) Comparison between the reference law and Bridgman's prediction when changing the specimen portion to be fitted with a 3rd order polynomial. In (**b**,**c**) $\varepsilon_{eq,pl,avg}$ refers to the averaged value at the minimum cross-section of the last configuration analyzed (according to FE simulation of the reference law).

### 4.3. Proposed Method

The same experimental necking configurations of Section 4.1 were considered, and the proposed procedure was applied as described in Section 2. Actually, when searching within the database for the best numerical shape, the authors just considered the portion of the experimental semi-profile satisfying the condition $2\ln(r_0/r) > \varepsilon_n$ (so this region coincides with Region 1 of Section 4.2).

Some of the experimental deformed shapes are shown in Figure 7a, where the horizontal line limits the portion of the specimen considered when searching for the best numerical profile. In Figure 7a, the best numerical profiles found in the database are plotted too; it can be seen that they fit very well the experimental shape within the region considered. This highlights that the approach proposed in this paper offers a different way to interpolate

the experimental profile for removing non-physical oscillations: not with a mathematical function, but with a curve (one of the database profiles) that really represents a necking shape. For sake of comparison, the profiles predicted by the reference law are shown too.
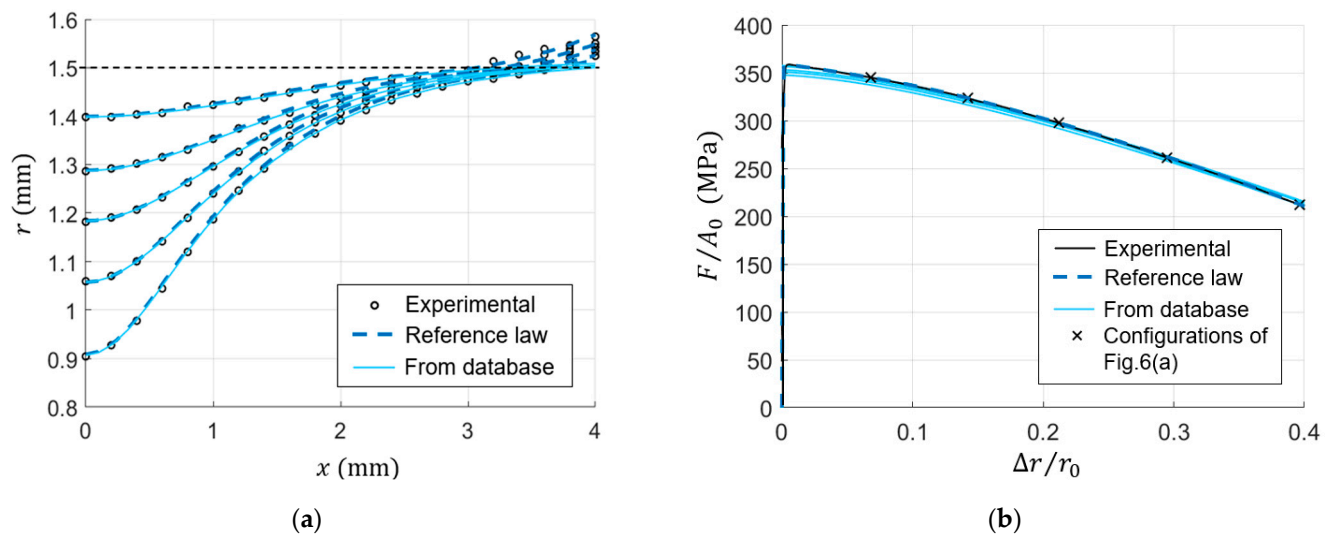


(**a**)

(**b**)

**Figure 7.** Results of the proposed method on pure copper. (**a**) Comparison between some experimental semi-profiles, the best ones found in the database, and the ones predicted by the reference law. (**b**) Comparison of the engineering curves (in terms of radial contraction at the minimum cross-section): the experimental one, those from the database, and the one predicted by the reference law.

In Figure 7b, a comparison in terms of engineering curve is presented too and the goodness of the results is suggested by the fact that the engineering curves from the database, properly modified, are close to each other and to the experimental one.

The series of all identified hardening laws is shown in Figure 8a. Each curve is plotted for the range of strains $[\varepsilon_{min}; \varepsilon_{max}]$ reached on the specimen surface within a fixed distance from the necking center. This distance was determined as the axial portion satisfying the condition $2\ln(r_0/r) > \varepsilon_n$ at the first configuration analyzed. The identified laws are characterized by a maximum discrepancy of about 3.6% (evaluated as the variability of the predicted stress at $\varepsilon_{min}$). In Figure 8b the corresponding uncertainty region is highlighted in gray and appears to be in an acceptable neighborhood of the reference law. Moreover, the uncertainty is much lower than that associated with Bridgman's correction (see Figure 6c).

Different strategies could be adopted to determine a unique material hardening law from the series of curves. In this paper, it was chosen to join the points of $\varepsilon_{max}$ of the different configurations analyzed (marked with this symbol | in Figure 8a) and consider it as the material hardening law. In Figure 8b, such law is compared to the reference one (predicted by the FE-based inverse method) and to the laws predicted by the analytical methods. The analytical methods considered were Bridgman's and Gromada's formula (Equation (4) and Equation (5) respectively). The former as it is still widely used, the latter as it provides an improvement of the previous one still based on local curvature measurements. In both cases, the curvature was estimated as the curvature at the necking center of a fourth order polynomial fitting Region 1 (see first plot of Figure 6a).
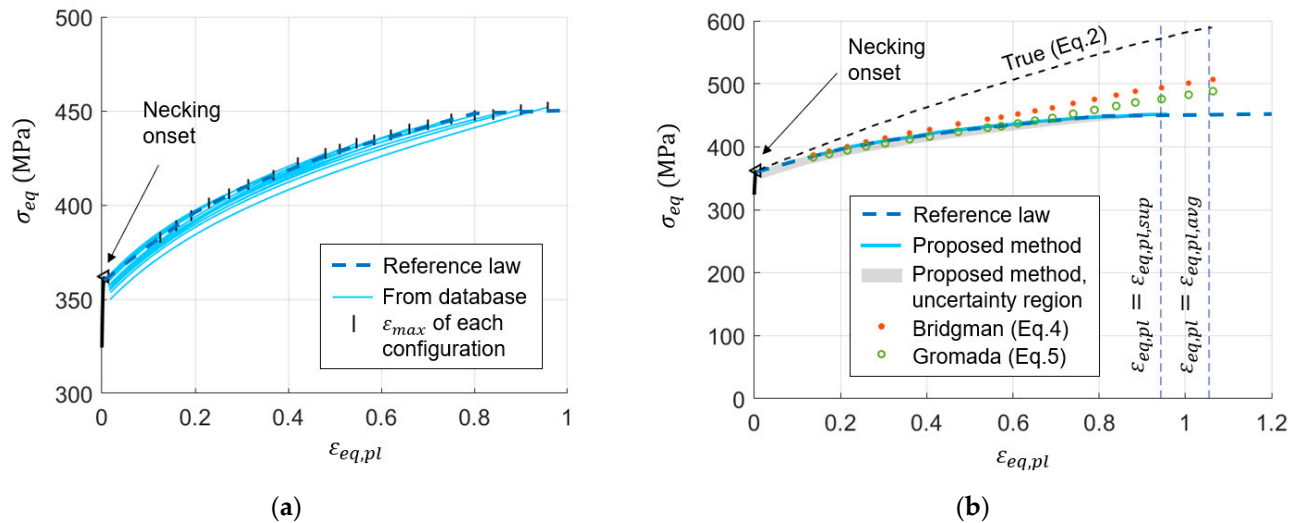
(**a**)



(**b**)

**Figure 8.** Results of the proposed method on pure copper. (**a**) Series of identified hardening laws with markers at the maximum equivalent plastic strain achieved on the specimen surface at each configuration. (**b**) Comparison between the material hardening law (obtained by joining the points of maximum deformation), its uncertainty region, the reference law, Bridgman's and Gromada's predictions (4th order polynomial on Region 1).

The results of the proposed method well agree with the reference law also at large strains, where instead other methods have a higher error (even if Gromada's results are better than Bridgman's). The advantage with respect to other corrections is also a more robust procedure, thanks to the fact that at different time instants the whole shape is analyzed. Thus, not only a point of the hardening law is obtained at each instant, but a part of the post-necking curve.

## 5. Preliminary Application to a Strain-Rate Sensitive Material

The necking response, even during a quasi-static tensile test, could be affected by strain-rate, in cases where the material is sufficiently sensitive to this variable. Indeed, during necking the material experiences a non-uniform strain-rate distribution, with maximum values that may even be an order of magnitude higher than the nominal strain-rate of the test. There are materials, such as copper analyzed in Section 4, which do not exhibit strain-rate sensitivity within quasi-static tests. However, there are also materials, such as pure molybdenum, that are highly sensitive to strain-rate at low strain-rates [27,40]. In these cases, the strain-rate variation and non-uniformity that characterizes necking causes the quasi-static response to be affected by the strain-rate.

Therefore, a quasi-static tensile test on pure molybdenum was conducted according to Section 3 and was used as another case study. The aim was to analyze the information that could be gained from applying the proposed method to a strain-rate sensitive material. For reference, the hardening law and strain-rate sensitivity was firstly identified with a FE-based inverse method. The material isotropy was verified as explained in Section 4.

### 5.1. Reference Law

The FE-based inverse method used to identify the hardening law is analogous to the one presented for pure copper in Section 4.1. Thus, the cost function to be minimized is the force at given increments of radial contraction. The same FE model was used, except for the material model because now the strain-rate sensitivity should be taken into account. A

Johnson–Cook model was chosen (implemented as *MAT_015 in Ansys LS-DYNA). Since no thermal effects are present in quasi-static tests, the flow stress equation is:

$$\sigma_{eq} = \left( A + B\varepsilon_{eq,pl}^{n} \right)\left( 1 + C \ln \frac{\dot{\varepsilon}_{eq,pl}}{\dot{\varepsilon}_0} \right) \tag{6}$$

where $A$, $B$, $n$, $C$ were considered as optimization variables.

The resulting law will be used for critically analyzing the results of the proposed method. It can be considered as reference because FE simulations allow for adequate consideration of the specimen geometry and spatial distributions of the strain, strain-rate, and stress. A further proof of the accuracy of the identified law is its capability to adequately reproduce the experimental test, in terms of both the necking shape (as will be shown in Figure 9a) and the engineering curve (as will be shown in Figure 9b).
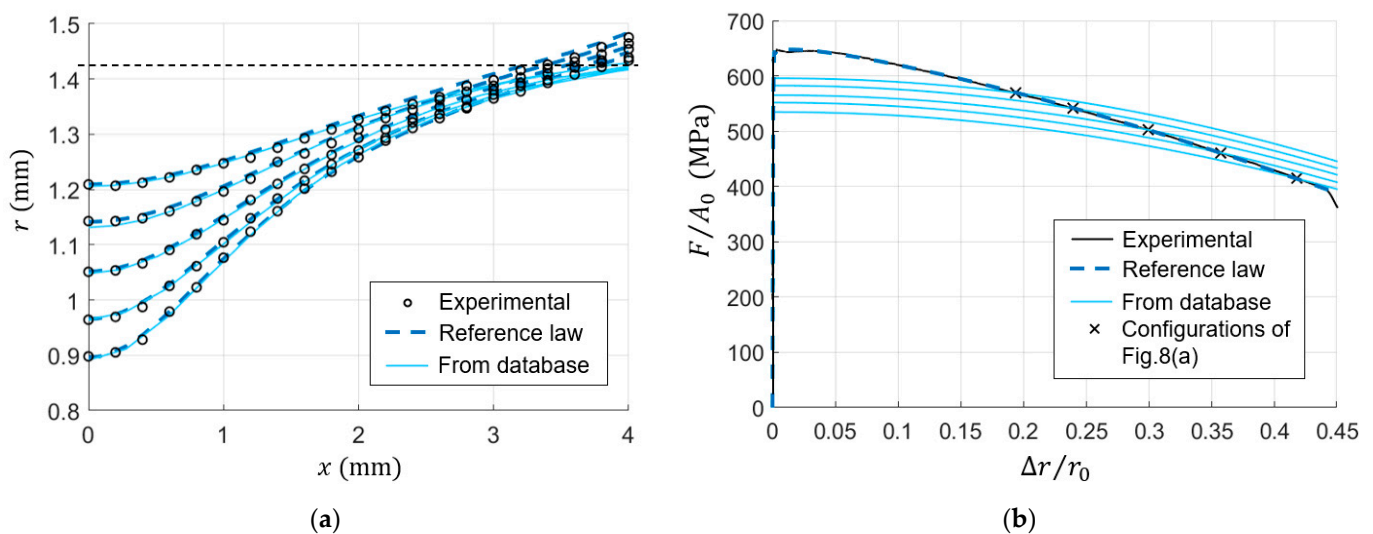


(**a**)



(**b**)

**Figure 9.** Results of the proposed method on pure molybdenum. (**a**) Comparison between some experimental semi-profiles, the best ones found in the database, and the ones predicted by the reference law. (**b**) Comparison of the engineering curves (in terms of radial contraction at the minimum cross-section): the experimental one, those from the database, and the one predicted by the reference law.

*5.2. Proposed Method*

The proposed method was applied to a series of configurations. Some of the deformed profiles considered are shown in Figure 9a, in comparison with the best shapes found in the database (again just the experimental portion verifying $2\ln(r_0/r) > \varepsilon_n$ was considered). A good agreement can be seen for the different configurations. However, when looking at the engineering curves in Figure 9b it is possible to see that none of the curves from the database well approximates the experimental one. This is because material models considered in the database are not strain-rate sensitive. A single law from the database is able to properly catch the material behavior in a surrounding of the corresponding configuration, but not in the whole test.

Nevertheless, the FE database can still provide useful information about each deformed configuration, in particular the strain-rate distribution on the specimen surface in the different configurations analyzed, as shown in Figure 10a. This figure also highlights the non-uniformity of the strain-rate experienced during necking.

Material strain-rate dependence explains why the identified hardening laws exhibit a relevant discrepancy when looking at $\sigma_{eq} - \varepsilon_{eq,pl}$, as observable from the gray region in Figure 10b. Indeed, a 2D view of the hardening law is not adequate, but an additional axis should be considered to take strain-rate into account. Thus, the result of applying the

proposed procedure is a point cloud in the strain, strain-rate, and stress space that represent points of the surface $\sigma_{eq}\left(\varepsilon_{eq,pl}, \dot{\varepsilon}_{eq,pl}\right)$.

For building the gray region, each of the identified hardening laws was considered just for the range $[\varepsilon_{min}; \varepsilon_{max}]$ of the strains for which it is valid. Connecting the points of maximum deformation of the different identified laws, it was possible to predict the path followed in the plane $\sigma_{eq} - \varepsilon_{eq,pl}$ by the point at the necking center on the sample surface. Figure 10b shows that this path agrees with FE predictions. For test conditions and/or materials in which strain-rate dependence can be neglected, all the material points follow the same path on $\sigma_{eq} - \varepsilon_{eq,pl}$ plane (until they undergo elastic unloading) [26]. This is why, in such cases, the series of laws identified with the proposed method are theoretically overlapped with each other. If the path followed by different points is different, then such laws deviate considerably, one with respect to the other. This is actually what happened in the experimental case under analysis (paths followed by different superficial points are shown with dotted lines in Figure 10b). More generally, this happens in cases of strain-rate sensitivity: different material points may experience the same strains but at different strain-rates and thus at different stresses.
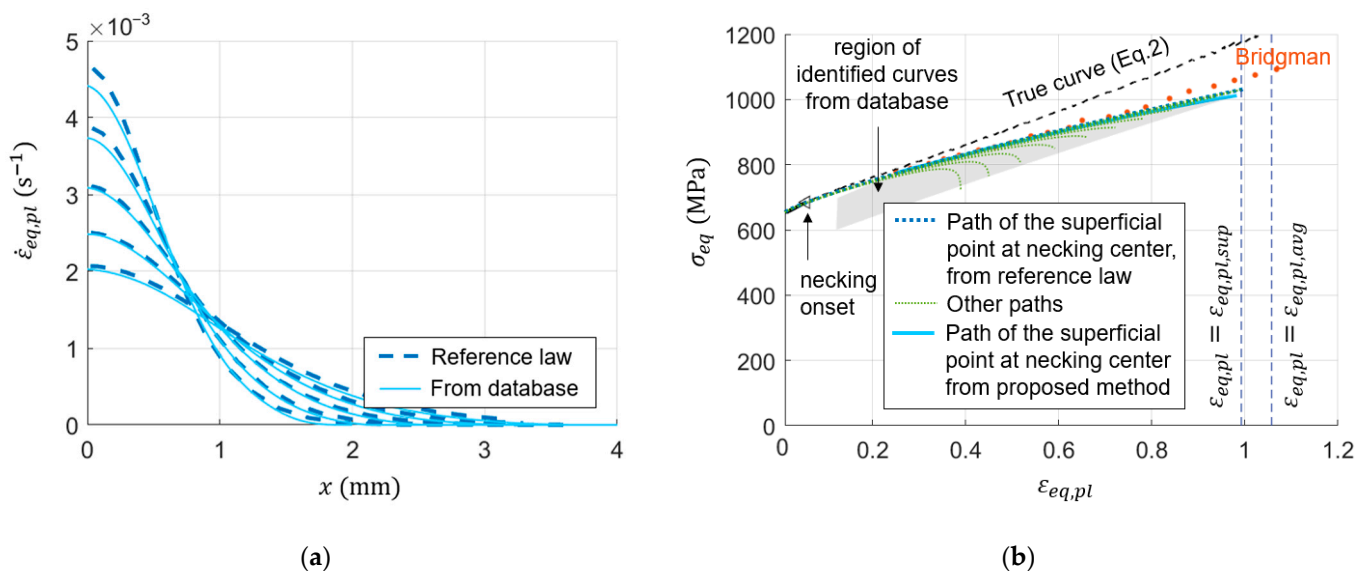


(**a**)  (**b**)

**Figure 10.** Results of the proposed method on pure molybdenum. (**a**) Strain-rate distribution at the same configurations of Figure 9: comparison between the prediction of the reference law and the proposed method. (**b**) Comparison of the path of the superficial point at the necking center according to the prediction of the reference law and of the proposed method (obtained by joining the points of maximum deformation). The paths of other superficial points according to the reference law are plotted too. For the proposed method, the gray region represents the locus of $\left(\varepsilon_{eq,pl}, \sigma_{eq}\right)$ of all the superficial points for all the considered configurations. For sake of comparison, also Bridgman's prediction (4th order polynomial on Region 1) is presented.

In Figure 10b, Bridgman's correction is reported too, this was estimated by considering a fourth order polynomial for fitting the specimen region that verifies the condition $2\ln(r_0/r) > \varepsilon_n$. However, no hint about strain-rate sensitivity is obtained and one may wrongly consider this to be the hardening law.

Conversely, the proposed method can highlight a strain-rate dependence of the material. This is a result of having considered the whole shape and not just the necking center. Moreover, the strategy presented in this paper identifies a series of points in the strain, strain-rate, and stress space that represent points of the surface $\sigma_{eq}\left(\varepsilon_{eq,pl}, \dot{\varepsilon}_{eq,pl}\right)$.

Future endeavors will be dedicated to understanding how the information obtained from the database could be further exploited for characterizing strain-rate sensitive materials.

## 6. Conclusions

In the present paper, the authors have proposed a method to efficiently calibrate strain hardening laws at large deformation by exploiting the post-necking part of tensile tests. This is important because the greater part of tensile tests on ductile metals occurs in necking phase.

It is possible to conceive of the proposed method as an evolution of Bridgman's theory that takes into account the whole shape via a database approach. From a single shape, Bridgman's correction looks at the necking center and determines a single point of the hardening law. This is valid also for all analytical approaches based on the necking center geometry. However, each shape is representative of a portion of the plastic flow curve (and not just of a point), and the proposed method is able to determine this information. The knowledge gained from subsequent images generates redundancy, thus increasing the overall stability and robustness of the method. Furthermore, the accuracy is improved with respect to analytical corrections because no simplifying hypothesis on stress and strain states are considered; instead, a database collecting FE results is exploited.

Applying the proposed method to an experimental tensile test on pure copper has shown its better accuracy and robustness with respect to Bridgman's approach. Moreover, the computational effort is comparable to that of analytical approaches since a database is employed. Finally, the experimental effort is limited because the specimen external profile is used and no information of a small portion around the necking center nor DIC measurements are needed. A telecentric optical bench was used to ensure accurate measurement of the external contour.

A preliminary analysis has also been conducted to test the proposed method on a strain-rate sensitive material, pure molybdenum. The results have shown that the method may allow the detecting of the material strain-rate sensitivity and the determination of a series of points on the hardening surface. Such promising results suggest that strain-rate sensitive materials could be successfully analyzed by means of adequate datasets, and future efforts will be devoted to further investigate this possibility.

## References

1. Considère, M. *Mémoire sur l'Emploi du fer et de l'Acier dans les Constructions*; Dunod: Paris, France, 1885.
2. Tu, S.; Ren, X.; He, J.; Zhang, Z. Stress–strain curves of metallic materials and post-necking strain hardening characterization: A review. *Fatigue Fract. Eng. Mater. Struct.* **2020**, *43*, 3–19. [CrossRef]
3. Gupta, M.K.; Singh, N.K. Post Necking Behaviour and Hardening Characterization of Mild Steel. *Solid State Phenom.* **2021**, *319*, 7–12. [CrossRef]
4. Zhu, L.; Huang, X.; Liu, H. Study on constitutive model of 05Cr17Ni4Cu4Nb stainless steel based on quasi-static tensile test. *J. Mech. Sci. Technol.* **2022**, *36*, 2871–2878. [CrossRef]

5.  Bridgman, P.W. *Studies in Large Plastic Flow and Fracture*; Metallurgy and metallurgical engineering series; McGraw Hill: New York, NY, USA, 1952.
6.  Murata, M.; Yoshida, Y.; Nishiwaki, T. Stress correction method for flow stress identification by tensile test using notched round bar. *J. Mater. Process. Technol.* **2018**, *251*, 65–72. [CrossRef]
7.  La Rosa, G.; Risitano, A.; Mirone, G. Postnecking elastoplastic characterization: Degree of approximation in the Bridgman method and properties of the flow-stress/true-stress ratio. *Metall. Mater. Trans. A* **2003**, *34*, 615–624. [CrossRef]
8.  Mirone, G.; Verleysen, P.; Barbagallo, R. Tensile testing of metals: Relationship between macroscopic engineering data and hardening variables at the semi-local scale. *Int. J. Mech. Sci.* **2019**, *150*, 154–167. [CrossRef]
9.  Gromada, M.; Mishuris, G.; Öchsner, A. *Correction Formulae for the Stress Distribution in Round Tensile Specimens at Neck Presence*; Springer Science & Business Media: Berlin/Heidelberg, Germany, 2011.
10. Nie, X.; Song, B.; Loeffler, C.M. A novel splitting-beam laser extensometer technique for Kolsky tension bar experiment. *J. Dyn. Behav. Mater.* **2015**, *1*, 70–74. [CrossRef]
11. Yu, J.H.; McWilliams, B.A.; Kaste, R.P. Digital image correlation analysis and numerical simulation of aluminum alloys under quasi-static tension after necking using the Bridgman's correction method. *Exp. Tech.* **2016**, *40*, 1359–1367. [CrossRef]
12. Sancho, A.; Cox, M.J.; Cartwright, T.; Davies, C.M.; Hooper, P.A.; Dear, J.P. An experimental methodology to characterise post-necking behaviour and quantify ductile damage accumulation in isotropic materials. *Int. J. Solids Struct.* **2019**, *176*, 191–206. [CrossRef]
13. Lu, F.; Mánik, T.; Lægreid Andersen, I.; Holmedal, B. A Robust Image Processing Algorithm for Optical-Based Stress–Strain Curve Corrections after Necking. *J. Mater. Eng. Perform.* **2021**, *30*, 4240–4253. [CrossRef]
14. Siegmann, P.; Alén-Cordero, C.; Sánchez-Montero, R. Experimental approach for the determination of the Bridgman's necking parameters. *Meas. Sci. Technol.* **2019**, *30*, 114003. [CrossRef]
15. Chen, B.; Pan, B. Measuring true stress–strain curves of cylindrical bar samples with mirror-assisted multi-view digital image correlation. *Strain* **2022**, *58*, e12403. [CrossRef]
16. Versaillot, P.D.; Wu, Y.F.; Zhao, Z.L. Experimental study on the evolution of necking zones of metallic materials. *Int. J. Mech. Sci.* **2021**, *189*, 106002. [CrossRef]
17. Le Roy, G.; Embury, J.D.; Edwards, G.; Ashby, M.F. A model of ductile fracture based on the nucleation and growth of voids. *Acta Metall.* **1981**, *29*, 1509–1522. [CrossRef]
18. Lu, F.; Mánik, T.; Holmedal, B. Stress corrections after necking using a two-parameter equation for the radius of curvature. *J. Appl. Mech.* **2021**, *88*, 061006. [CrossRef]
19. Mirone, G. A new model for the elastoplastic characterization and the stress–strain determination on the necking section of a tensile specimen. *Int. J. Solids Struct.* **2004**, *41*, 3545–3564. [CrossRef]
20. Zhao, K.; Wang, L.; Chang, Y.; Yan, J. Identification of post-necking stress–strain curve for sheet metals by inverse method. *Mech. Mater.* **2016**, *92*, 107–118. [CrossRef]
21. Pham, Q.T.; Nguyen-Thoi, T.; Ha, J.; Kim, Y.S. Hybrid fitting-numerical method for determining strain-hardening behavior of sheet metals. *Mech. Mater.* **2021**, *161*, 104031. [CrossRef]
22. Yao, Z.; Wang, W. Full-range strain-hardening behavior of structural steels: Experimental identification and numerical simulation. *J. Constr. Steel Res.* **2022**, *194*, 107329. [CrossRef]
23. Zeng, X.; Huo, J.S. Rate-dependent constitutive model of high-strength reinforcing steel HTRB600E in tension. *Constr. Build. Mater.* **2023**, *363*, 129824. [CrossRef]
24. Zhang, H.; Xu, C.; Gao, T.; Li, X.; Song, H. Identification of strain hardening behaviors in titanium alloys using tension tests and inverse finite element method. *J. Mech. Sci. Technol.* **2023**, *37*, 3593–3599. [CrossRef]
25. Peroni, L.; Scapin, M. Strength Model Evaluation Based on Experimental Measurements of Necking Profile in Ductile Metals. *EPJ Web Conf.* **2018**, *183*, 01015. [CrossRef]
26. Beltramo, M.; Scapin, M.; Peroni, L. An advanced post-necking analysis methodology for elasto-plastic material models identification. *Mater. Des.* **2023**, *230*, 111937. [CrossRef]
27. Scapin, M.; Peroni, L.; Carra, F. Investigation and mechanical modelling of pure molybdenum at high strain-rate and temperature. *J. Dyn. Behav. Mater.* **2016**, *2*, 460–475. [CrossRef]
28. Scapin, M.; Peroni, L.; Torregrosa, C.; Perillo-Marcone, A.; Calviani, M. Effect of strain-rate and temperature on mechanical response of pure tungsten. *J. Dyn. Behav. Mater.* **2019**, *5*, 296–308. [CrossRef]
29. Kajberg, J.; Lindkvist, G. Characterisation of materials subjected to large strains by inverse modelling based on in-plane displacement fields. *Int. J. Solids Struct.* **2004**, *41*, 3439–3459. [CrossRef]
30. Gross, A.J.; Ravi-Chandar, K. On the extraction of elastic–plastic constitutive properties from three-dimensional deformation measurements. *J. Appl. Mech.* **2015**, *82*, 071013. [CrossRef]
31. Zhang, H.; Coppieters, S.; Jiménez-Peña, C.; Debruyne, D. Inverse identification of the post-necking work hardening behaviour of thick HSS through full-field strain measurements during diffuse necking. *Mech. Mater.* **2019**, *129*, 361–374. [CrossRef]
32. Kim, J.H.; Serpantié, A.; Barlat, F.; Pierron, F.; Lee, M.G. Characterization of the post-necking strain hardening behavior using the virtual fields method. *Int. J. Solids Struct.* **2013**, *50*, 3829–3842. [CrossRef]
33. Coppieters, S.; Kuwabara, T. Identification of post-necking hardening phenomena in ductile sheet metal. *Exp. Mech.* **2014**, *54*, 1355–1371. [CrossRef]

34. Park, J.S.; Kim, J.M.; Barlat, F.; Lim, J.H.; Pierron, F.; Kim, J.H. Characterization of dynamic hardening behavior at intermediate strain rates using the virtual fields method. *Mech. Mater.* **2021**, *162*, 104101. [CrossRef]

35. Tvergaard, V.; Needleman, A. Analysis of the cup-cone fracture in a round tensile bar. *Acta Metall.* **1984**, *32*, 157–169. [CrossRef]

36. Scapin, M.; Peroni, L.; Fichera, C. Investigation of dynamic behaviour of copper at high temperature. *Mater. High Temp.* **2014**, *31*, 131–140. [CrossRef]

37. Zhang, H.; Li, X.; Gao, T.; Song, H.; Huang, G. Experimental study on deformation evolution and fracture behaviors of pure titanium at different stress triaxialities. *Eng. Fract. Mech.* **2021**, *258*, 108127. [CrossRef]

38. Arthur, D.; Vassilvitskii, S. k-means++: The advantages of careful seeding. In Proceedings of the SODA '07: Proceedings of the Eighteenth Annual ACM-SIAM Symposium on Discrete Algorithms, New Orleans, LA, USA, 7–9 January 2007; Volume 7, pp. 1027–1035.

39. Follansbee, P.S. *Fundamentals of Strength*; John Wiley & Sons, Inc.: Hoboken, NJ, USA, 2014; Volume 10, p. 9781118808412.

40. Chen, S.; Li, W.B.; Wang, X.M.; Yao, W.J.; Song, J.P.; Jiang, X.C.; Yan, B.Y. Comparative Study of the Dynamic Deformation of Pure Molybdenum at High Strain Rates and High Temperatures. *Materials* **2021**, *14*, 4847. [CrossRef]